VASCO: Volume and Surface Co-Decomposition for Hybrid Manufacturing

ANONYMOUS AUTHOR(S)
SUBMISSION ID: 232

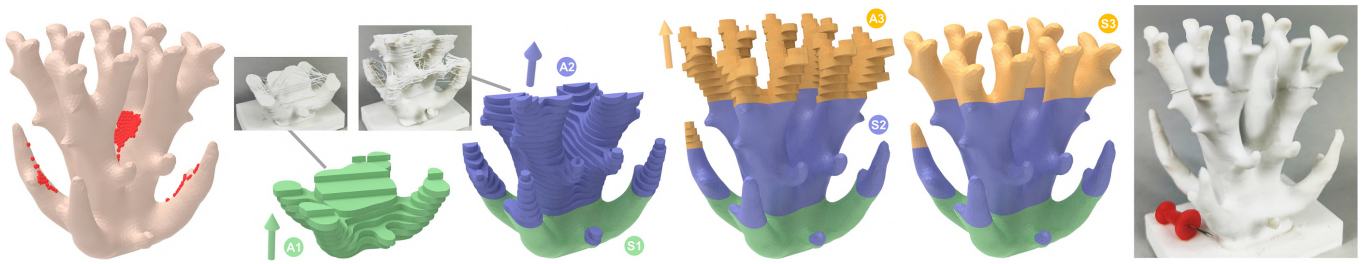

Fig. 1. The proposed work introduces a novel computational framework that aims to minimize the number of transitions between additive and subtractive manufacturing processes while ensuring tool accessibility in manufacturing a complex object. This figure shows the *Coral* model, presumerably manufactured additively, has surface regions that cannot be reached by any subtractive cutter (represented by red dots in the leftmost figure). To address the tool accessibility constraints, the *Coral* model is divided into three components, corresponding to three interleaving manufacturing steps, referred to as "AM-then-SM." These steps produce volume and surface segmentation, resulting in the creation of hybrid-fabricable blocks (represented by the green, blue, and yellow regions). The additive and subtractive manufacturing sequence of the *Coral* model is visualized using numbered labels in sequential order, such as $\{A1, S1, A2, S2, A3, S3\}$. The print directions for the hybrid-fabricable blocks are indicated by arrows. The right image displays the physical fabrication outcome of the *Coral* model. It demonstrates that the proposed framework, known as ASHM (Additive-Subtractive Hybrid Manufacturing), can enhance surface quality, especially for inaccessible surfaces, by leveraging the combined strengths of additive and subtractive manufacturing techniques to fabricate complex geometries.

Additive and subtractive hybrid manufacturing (ASHM) involves the alternating use of additive and subtractive manufacturing techniques, which provides unique advantages for fabricating complex geometries with otherwise inaccessible surfaces. However, a significant challenge lies in ensuring tool accessibility during both fabrication procedures, as the object shape may change dramatically, and different parts of the shape are interdependent. In this study, we propose a computational framework to optimize the planning of additive and subtractive sequences while ensuring tool accessibility. Our goal is to minimize the switching between additive and subtractive processes to achieve efficient fabrication while maintaining product quality. We approach the problem by formulating it as a Volume-And-Surface-CO-decomposition (VASCO) problem. First, we slice volumes into slabs and build a dynamic-directed graph to encode manufacturing constraints, with each node representing a slab and direction reflecting operation order. We introduce a novel geometry property called hybrid-fabricability for a pair of additive and subtractive procedures. Then, we propose a beam-guided top-down block decomposition algorithm to solve the VASCO problem. We apply our solution to a 5-axis hybrid manufacturing platform and evaluate various 3D shapes. Finally, we assess the performance of our approach through both physical and simulated manufacturing evaluations.

CCS Concepts: • **Computing methodologies** → **Shape modeling**; *Graphics systems and interfaces.*

Permission to make digital or hard copies of all or part of this work for personal or classroom use is granted without fee provided that copies are not made or distributed for profit or commercial advantage and that copies bear this notice and the full citation on the first page. Copyrights for components of this work owned by others than the author(s) must be honored. Abstracting with credit is permitted. To copy otherwise, or republish, to post on servers or to redistribute to lists, requires prior specific permission and/or a fee. Request permissions from permissions@acm.org.
© 2023 Copyright held by the owner/author(s). Publication rights licensed to ACM.
0730-0301/2023/12-ART $15.00
https://doi.org/10.1145/3618324

Additional Key Words and Phrases: Surface decomposition, volume decomposition, sequence planning, hybrid manufacturing

ACM Reference Format:
Anonymous Author(s). 2023. VASCO: Volume and Surface Co-Decomposition for Hybrid Manufacturing. *ACM Trans. Graph.* 42, 6 (December 2023), 17 pages. https://doi.org/10.1145/3618324

1 INTRODUCTION

The computer graphics community has raised a growing interest in both additive manufacturing (AM) and subtractive manufacturing (SM), especially 3D printing and CNC machining [Bartoň et al. 2021; Bickel et al. 2018; Martínez et al. 2017; Zhao et al. 2018]. However, few works have considered combining both's capabilities, leveraging 3D printing's strength in fabricating complex geometries with high material utilization and CNC machining's strengths in high machining precision and high-quality surface finishes. Such hybrid manufacturing technology is called **additive/subtractive hybrid manufacturing (ASHM)** [Dilberoglu et al. 2021]. Pure additive manufacturing features near-net-shape fabrication with minimal material waste, but its accuracy and surface quality may not be suitable for precision engineering. Compared to 3D printing, ASHM would remove the staircase artifact raised by layered fabrication and realize higher product precision with superior surface finishes. However, post-processing inaccessible surfaces with a simple additive-then-post-smoothing process, like post-CNC machining, can be difficult. While abrasive flow machining (AFM) can be used, it may cause random shape changes or undetectable structural damage and cannot guarantee fabrication precision. Furthermore, current 3D printing is believed to be one order of magnitude less precise than CNC machining, and simply increasing resolution is

(a) injection mold[1] (b) exhaust manifold[2] (c) impeller[3]

Fig. 2. The typical applications of ASHM. The intricate inner surfaces of the channels in injection molds (a) and exhaust manifolds (b) significantly enhance heat dissipation efficiency and increase exhaust velocity due to their high dimensional accuracy. The use of high-precision free-form surfaces in the impeller (c) is crucial in minimizing vibration and noise levels.

insufficient to meet precision requirements. In contrast to CNC machining, ASHM is more flexible in manufacturing complicated structural parts with radical geometries. Therefore, interchanging between AM and SM to form the ASHM strategy is superior to the AM technique alone. Typical applications of ASHM include device parts for computational photography, microfluidic devices with precise internal channels, injection molds with conformal cooling channels, exhaust manifold, and engine heat exchangers with regenerative cooling channels [Behandish et al. 2018; Dezaki et al. 2022]; see Figure 2. However, hybrid manufacturing has to simultaneously consider computational geometry processes from additive and subtractive manufacturing, which are far from fully automatic, particularly for general complex geometries [Chen et al. 2018b].

Hybrid manufacturing, which combines additive manufacturing (AM) and subtractive machining (SM), utilizes a print head to construct 3D volumes through layered material deposition (each layer is a slicing planar of the object)[4], while employing a CNC machining cutter to remove material from a 3D surface by following designated spatial curves. The ASHM (Additive-Subtractive Hybrid Manufacturing) platform, as depicted in Figure 1, facilitates multi-directional 3D printing and 5-axis milling, thus providing enhanced movement flexibility. In this study, we adopt the ASHM platform, and the manufacturing process entails a series of "AM-then-SM" stages. Within each stage, the print head initially generates a 3D solid volume, which is then subjected to a surface machining step to sculpt the corresponding 3D surface of the additive 3D volume. A critical aspect of the process is ***Sequence planning***, which involves determining the alternating sequence $\{A1, S1, A2, S2, ..., An, Sn\}$, where A and S represent additive and subtractive steps, respectively [Chen et al. 2018b].

The primary objective of sequence planning in hybrid manufacturing is to minimize the number of "AM-then-SM" switches. Each switch involving A_i or S_i necessitates recalibration and specific pre-processing of the print head or CNC cutter, which can have a substantial impact on manufacturing efficiency. Furthermore, the locations where process switching occurs often result in undesired

[1]Hong Kong Productivity Council (HKPC), https://www.innovationhub.hk/article/3d-conformal-cooling-mould
[2]https://caautoparts.com/products/tm-4afe-s-t25
[3]HILLTOP, https://www.pinterest.jp/pin/311733605430810230/
[4]This paper defines the concept of a *slab* to refer to the portion between two consecutive planar layers.

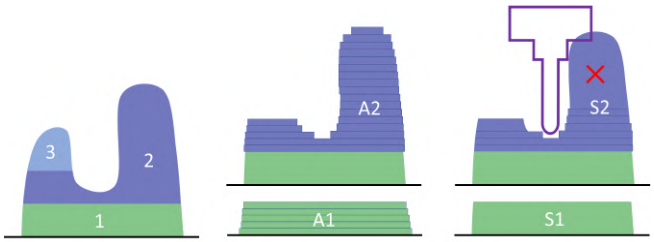

(a) (b) (c)

Fig. 3. The figure illustrates the 2D shape being decomposed into three regions (a). (b) shows the AM process followed by the two regions' SM process (c), supposing the print head and machining cutter can only point downward. The first green region is a hybrid-fabricable block, that can be successfully manufactured. However, for the second blue region 2, collisions occur between the tool and the upper right corner of the model during the subtractive process when reaching the concave area. As a result, it cannot be considered as a block.

finishing artifacts, thereby affecting both surface quality and manufacturing precision. Hence, an optimal sequence planning strategy aims to minimize process switches while considering machining efficiency and product quality. However, it is worth noting that this problem is inherently challenging, as demonstrated by the NP-hardness of single volume decomposition [FEKETE and MITCHELL 2001]. Providing a formal NP-hardness proof for this specific problem lies outside the scope of our work. As we know, no existing works address this problem to general sequence planning scenarios without restrictions on the target shapes, the hybrid sequence cycles, or manufacturing degrees of freedom [Behandish et al. 2018; Chen et al. 2020, 2018b; Harabin and Behandish 2022; Liu et al. 2019a].

The key challenge in sequence planning for hybrid manufacturing lies in the significant shape transformations that occur at each "AM-then-SM" stage, leading to dynamic changes in tool accessibility. These variations pose considerable complexity to the sequence planning process. It is imperative that each A or S manufacturing process adheres to tool accessibility constraints and manufacturing dependency constraints. Tool accessibility constraints ensure that the print head or CNC cutter avoids collisions with the realized shape and the ASHM machine itself. Additionally, manufacturing operations must respect precedence constraints, meaning that they cannot be executed before the completion of the prerequisite steps on which they rely. It is noteworthy that the formulation of these manufacturing constraints is discussed in detail in subsection 3.2.

In the ASHM process, AM and SM steps consistently alternate. Each AM stage in the ASHM sequence is responsible for producing specific 3D volumes, adhering to a predetermined set of print head directions. As a result, planning the sequence of AM steps equates to a volume decomposition challenge. Conversely, every SM phase involves machining distinct 3D surfaces based on a designated set of CNC cutter directions. This makes the planning of SM steps analogous to a surface decomposition issue. We formulate the joint optimization of AM (volume decomposition) and SM steps (surface decomposition) in ASHM sequence planning as the "Volume-And-Surface-CO-decomposition, VASCO" problem. Our

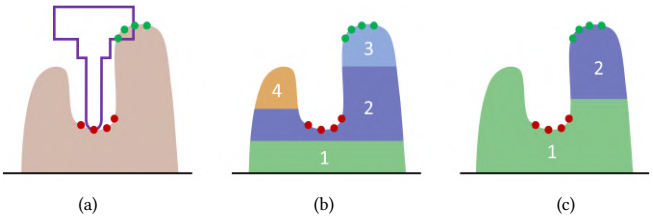

Fig. 4. One desired property of hybrid-fabricable block for shorting the ASHM sequence: the blocks realized in the early stages should include as many inaccessible regions as possible. In this illustration, we suppose the print head and machining cutter can only point downward. (a) The red dots represent the inaccessible areas that cannot be reached by the CNC cutter when machining on the entire object's surface, while the green dots indicate the areas that collide with the cutter. (b) In the scenario where the first green block excludes these inaccessible areas, it requires a total of 4 blocks. (c) In contrast, when the first green block includes these inaccessible areas, only 2 blocks are needed to manufacture the shape using ASHM.

key insight is that these two stages can be seamlessly integrated into a single optimization procedure. We introduce the concept of a *hybrid-fabricable block*, which refers to a pair of 3D volumes and surfaces that can be accessed by the respective manufacturing directions of ASHM, as illustrated in Figure 3. Hybrid-fabricability characterizes the property of such a block. The first green region represents a valid block, while the second blue region fails to meet the requirements due to collisions that occur during the subtractive manufacturing process. In this paper, we use the term "*block*" as an abbreviation for *hybrid-fabricable block* , the proposed solution to the VASCO problem aims to optimize the decomposition of *blocks* while considering both AM accessibility and SM accessibility.

We propose an iterative top-down decomposition algorithm to simplify the general VASCO problem. The top-down strategy has proved effective for multi-directional manufacturing [Chen et al. 2018b; Wu et al. 2020b]. It progressively decomposes a *fabricable sub-part* from the input shape until the entire shape is decomposed, where each iteration produces a block from the realized shape. Then, by reversing the order of decomposed blocks, a feasible ASHM manufacturing sequence is produced (see Figure 5).

The key technical challenge lies in how to produce one desired block which can be hybrid-fabricable for ASHM. Our solution is to encode all ASHM manufacturing constraints with a well-defined slab-based dynamic-directed graph, where each node is a slicing slab and edges between nodes are well-defined to formulate the tool accessibility and the manufacturing dependency constraints. Then, a block decomposition strategy is proposed by merging these slab nodes of the directed graph. We have observed that the selection of different AM directions for each block significantly affects the length of the sequence planning. Therefore, we develop a beam-guided search scheme to explore additional possibilities for ASHM direction selection. Furthermore, a set of block desired properties are introduced to help shorten the whole sequence (see one property in Figure 4). The beam-guided strategy can greatly enhance the local-optimum results achieved through a greedy scheme.

This paper applies these ideas to the 5-axis hybrid manufacturing platform where the machining cutter and print head rotate on the B and C rotation axes and move along X, Y, and Z in a linear direction. Such a 5-axis platform is mainly used for Directed Energy Deposition (DED) of metals. Given the platform's high degree of freedom, numerous viable manufacturing options exist, including flat or curved print layers, 3+2 or five-axis simultaneous machining strategies, support-free approaches, and the choice between manufacturing from scratch or utilizing existing parts. Covering all these options within a single paper is impractical. Hence, we focus on an initial attempt to investigate sequence planning scenarios at an appropriate level of complexity: support-free hybrid manufacturing from scratch, utilizing flat print slicing slabs and a 3+2 machining strategy. The efficiency of our VASCO algorithm is demonstrated through its application to diverse 3D target shapes, with an average execution time of approximately 6 minutes for moderately complex shapes. Physical and simulated hybrid manufacturing evaluations are also proposed, providing results that confirm the efficacy of our method in solving the ASHM sequence planning problem. Our solution exhibits sufficient generality to be extended to encompass other manufacturing options, with further discussion available in the result and conclusion sections.

2 RELATED WORK

This section first reviews the existing sequence planning works for ASHM, mainly from the mechanical field. Then we review the manufacturing-oriented shape decomposition frameworks proposed in the graphic domain, which can be grouped with and without considering manufacturing dependency constraints.

2.1 Sequence Planning for ASHM

ASHM techniques have experienced rapid development in recent years [Dezaki et al. 2022; Dilberoglu et al. 2021; Feldhausen et al. 2022; Flynn et al. 2016]. In line with the hardware advances, effective and efficient sequence planning is in high demand. There is significant progress on the sequence planning problem for ASHM from CAD/CAM community; however, the current state of hybrid manufacturing still falls short in fully exploiting the limitless potential offered by its capabilities. Most current hybrid process planning practices in engineering still rely on the operator's expertise. For example, commercial CAM software like SIEMENS NX supports AM and SM planning, but relies on the user to provide the sequences.

Sequence planning by search space restrictions. Due to the essential complexity of the sequence planning problem, existing methods mostly tackled the problem by imposing some restrictions, such that the dynamic ASHM accessibility and manufacturing dependency constraints can be simplified, and thus the solving space is shrunk. These works could be divided into three groups by what is restricted: 1) *target shapes*, include planar surfaces [Zhang et al. 2020], symmetric shapes [Chen and Frank 2019], shapes consisting of swept volumes [Xiao and Joshi 2020a], or columnar shapes [Chen et al. 2020, 2018b; Liu et al. 2019a]; 2) *A/S sequence cycles*, [Chen and Frank 2019] fixed the A/S sequence to only one cycle as S/A/S; 3) *manufacturing degrees of freedom (DOF)*, [Behandish et al. 2018; Chen et al. 2020, 2018b; Harabin and Behandish 2022] restricted the AM process with the fixed direction, or with an additional rotational

axis. In contrast, our work addresses the general sequence planning problem without these above restrictions.

Hybrid manufacturing-oriented Design. Design optimization for hybrid manufacturing is also considered in the literature [Liu et al. 2019b]. 2.5D machining features are inserted and treated as optimization primitives alongside the freeform structural topology optimization to ensure the post-machinability of quality-demanding surfaces. In [Liu and To 2016; Liu et al. 2019b], topology optimization is performed under the subtractive-first and then-additive remanufacturing strategy to create optimum product varieties for reusage. [Han et al. 2019] proposes a geometry approach for topology optimization of continuum structure. However, the current hybrid manufacturing-oriented design optimization mostly considers one AM-SM cycle, while the integration with a multiple-switching sequence is still an open problem.

2.2 Decomposition with dependency constraint

The shape decomposition problem considering manufacturing dependency constraints also exists in AM or SM. Depending on the fabrication element, it is tailored into volumetric- or layer-based decomposition.

Volumetric shape decomposition. Decomposing the given shape into a minimal number of sub-parts such that they are printed in different directions without support structures on a multi-directional 3+2-axis printing platform is a relevant problem to ours. It can be seen as the AM aspect of VASCO. Methods employ different strategies to solve this problem, like the flooding expansion algorithm that only works for simple topologies [Xu et al. 2019], or (accelerated) beam search for general shapes [Wu et al. 2020a,b]. They take a recursive downward search, i.e., the plane-clipping order is the inverse of the fabrication sequence. Especially in [Wu et al. 2020a,b], each clipping plane cuts the whole shape, which is a conservative choice for minimizing the number of sub-parts, such that the collision avoidance between the nozzle and realized workpiece is naturally satisfied. [Xiao and Joshi 2020b] consider multiple building directions for one sub-part to reduce the number of decomposed volumes. We got inspiration from these two ideas, i.e., downward search and multiple-plane in each local cutting. The difference is that we consider the dynamic change of the manufacturing constraints and encode them into a newly defined restricted graph, such that the search space is enlarged and the results are optimized.

Resembling the SM aspect of VASCO, [Mahdavi-Amiri et al. 2020] formulate the carvable volume decomposition problem for 3-axis CNC rough machining, to obtain a minimal set of carvable volumes with sequences. Similarly, we define the block that integrates both AM and SM constraints.

Layer-based decomposition. The sliced layer can also be regarded as an elementary of shape decomposition, where the shape decomposition is operated based on a layer-based graph [Kaplan et al. 2022; Zhong et al. 2022]. Specifically, [Zhong et al. 2022] focuses on optimizing toolpath continuity in the fabrication process of surface models using 3-axis 3D printers. To achieve this, they formulate the continuity optimization problem as a surface decomposition problem, wherein the surface model is decomposed into a minimum number of surface patches that can be printed continuously. To address this problem, the authors propose a bottom-up patch merging procedure that utilizes a unified graph of sliced layers to encode the additive accessibility constraint and printing order dependency. Similar to previous work, we use an over-decomposition layer-based graph to represent the search space. However, two key differences in our approach are that: 1) we consider subtractive constraint, and accordingly, we dynamically update two additional graphs during optimization; 2) our decomposition goals differ from the previous approach, which leads to different merging criteria. For multi-axis additive manufacturing, curved layers have advantages in achieving multiple objectives like support-free, strength reinforcement, and surface quality [Dai et al. 2018; Etienne et al. 2019; Fang et al. 2020; Zhang et al. 2022]. It works well on the platforms, especially with the control systems continuously moving all DOFs but with no dramatic change during material deposition.

2.3 Decomposition without dependency constraint

A majority of shape decomposition problems in manufacturing do not need to consider the manufacturing dependency constraint. In most scenarios, decomposition followed by assembly and with static rather than dynamic accessibility, like the divide-and-conquer strategy, has been widely applied to fulfill the target shapes effectively and efficiently while maximizing the fabrication capabilities.

Decomposition for additive manufacturing. The graphics domain has proposed many decomposition algorithms for additive manufacturing without any dependency constraints. For large object manufacturing, a minimal number of sub-parts are decomposed to assemble a large object [Chen et al. 2018a, 2015; Luo et al. 2012; Muntoni et al. 2018; Song et al. 2016]. To optimize the surface finish quality, researchers tailor the plane-cutting volume decomposition problem for minimizing support structures [Hu et al. 2014; Karasik et al. 2019], or decompose the object for reducing visual artifacts [Filoscia et al. 2020; Wang et al. 2016]. Multiple materials fabrication also leads to the shape decomposition problem, including the volume decomposition based on a given surface partition [Araújo et al. 2019; Liu et al. 2021].

Decomposition for molding and machining. Shape decomposition is also employed for fabricating freeform 3D objects with classical manufacturing techniques, such as surface decomposition for molding [Lin and Quang 2014; Malomo et al. 2016; Nakashima et al. 2018], volume decomposition for molding [Alderighi et al. 2021, 2019, 2018], height-field decomposition for machining [Herholz et al. 2015; Zhao et al. 2018] and volume decomposition for hot-wire cutting [Duenser et al. 2020]. The major difference between the above works with ours is that the split parts are also fabricated separately, with no manufacturing dependency constraints. Although assemblability constraints [Wang et al. 2021] or molding constraints [Alderighi et al. 2022], i.e., the collision avoidance among subparts, or even interlocking constraints [Chen et al. 2022] is taken into account, these methods can hardly be adapted to the VASCO problem, whose constraints are dynamic and among both parts and machine tools.

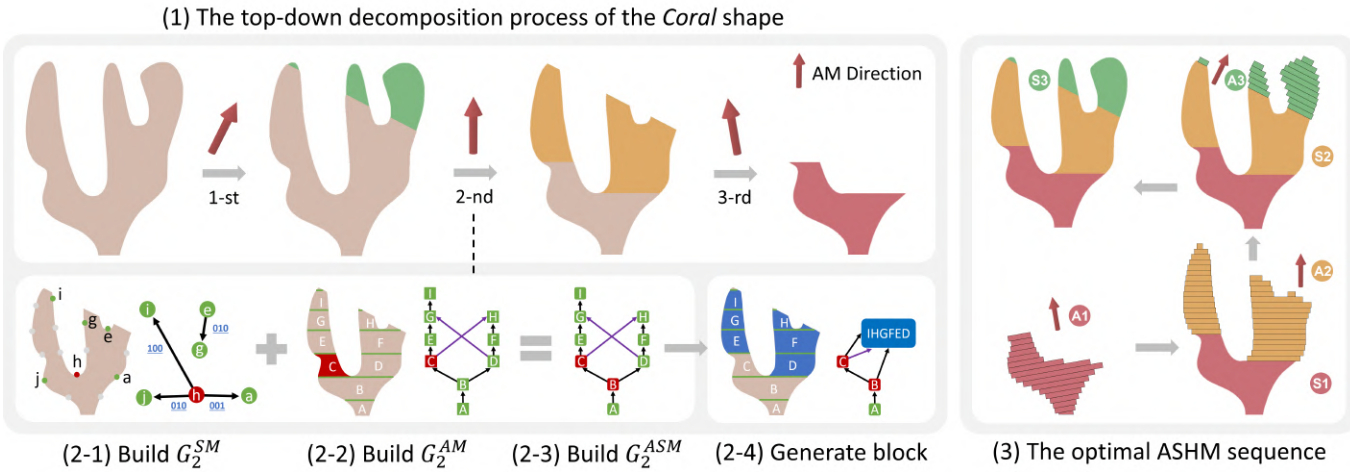

Fig. 5. We propose an iteration top-down decomposition algorithm for solving the VASCO problem. (1) It progressively decomposes a hybrid-fabricable block from the input *Coral* shape until the entire shape is decomposed. Each top-down decomposition iteration generates a hybrid-fabricable block with a randomly determined additive direction (deep red arrows). This figure shows three iterations, resulting in three blocks (the green, yellow, and red regions). (2) We visualize the procedure to produce one block of the 2nd iteration, where our solution is to encode all ASHM constraints with a well-defined slab-based dynamic-directed graph G_2^{ASM}, followed by a greed node merging process to generate blocks. To build G_2^{ASM} called a hybrid block graph, (2-1) we need first to build a subtractive block graph G_2^{SM} to encode the subtractive accessibility constraints, (2-2) and an additive block graph G_2^{AM} to encode the additive accessibility and dependency constraints. (2-3) Then integrate G_2^{SM} and G_2^{AM} to G_2^{ASM}. (2-4) The hybrid-fabricable block is generated based on G_2^{ASM} with a greed node merging algorithm. (3) Finally, by reversing the order of decomposed blocks, a feasible ASHM manufacturing sequence is produced.

3 OVERVIEW AND MANUFACTURING CONSTRAINTS

This section first restates the basic idea of our VASCO framework with an overview of our algorithm (Figure 5). Then clarifies the manufacturing constraints considered in ASHM sequence planning, i.e., additive accessibility, subtractive accessibility, manufacturing dependency constraint, and self-support constraint.

3.1 Algorithm Overview

Our algorithm takes as input a 3D object M represented by a boundary triangular mesh. We aim to generate the shortest fabrication sequence $\{A1, S1, A2, S2, ..., An, Sn\}$ to realize M by ASHM. Recall that we formulate the sequence planning problem as the "Volume-And-Surface-CO-decomposition, VASCO" problem, decomposing M into an ordered sequence of blocks $\mathbb{B} = \{B_1, B_2, ..., B_N\}$. Note that the sequence of blocks is reversed to the fabrication sequence. That is, each block B_i can be only manufactured once all the subsequent blocks $\{B_{i+1}, B_{i+2}, ..., B_N\}$ have been manufactured by ASHM. The optimization formulation of the VASCO problem is provided:

$$
\begin{aligned}
\min_{\mathbb{B}=\{B_1,B_2,...,B_N\}} \quad & N = |\mathbb{B}| \\
s.t. \quad & B_i = \{M_i, D_i^{AM}, D_i^{SM}\}, i = 1...N \\
& M_i = \partial M_i \cup \mho M_i, i = 1...N \\
& \mho M = \cup_{i=1}^{N} (\mho M_i) \\
& \partial M = \cup_{i=1}^{N} (\partial M_i) \\
& \mho M_i \cap \mho M_j = \partial M_i \cap \partial M_j = \emptyset, i \neq j, i, j = 1...N \\
& \mho M_i \text{ is fabricable by AM from } D_i^{AM}, i = 1...N \\
& \partial M_i \text{ is fabricable by SM from } D_i^{SM}, i = 1...N
\end{aligned}
\tag{1}
$$

where $\cup$ and $\cap$ indicate the *union* and *intersection* operators, separately. This paper uses ∂ to represent the outer surface of a 3D object, and $\mho$ is for the inner volume of a 3D object, $\mho M = M \setminus \partial M$. Each block B_i is associated with a specific sub-part of the input 3D object, represented as M_i. We refer $\cup_{j=i+1}^{N} M_j$ as the realized shape for M_i. While applying the "AM-then-SM" stage to realize M_i, no collisions are allowed with the realized shape $\cup_{j=i+1}^{N} M_j$ and the ASHM machine itself, including the print head and CNC cutter. The internal volume $\mho M_i$ is a self-support structure and fabricable using an AM process with a set of print head directions $D_i^{AM} = \{d_{i,1}^{AM}, d_{i,2}^{AM}, ..., d_{i,n}^{AM}\}$. Then its outer surface ∂M_i is carved by a subsequent SM process with a set of CNC cutter directions $D_i^{SM} = \{d_{i,1}^{SM}, d_{i,2}^{SM}, ..., d_{i,n}^{SM}\}$. As indicated, the outer surfaces or inner volumes of any two blocks must not overlap or have duplicates.

To address the VASCO optimization problem, we employ a heuristic iterative solution based on a top-down decomposition procedure. Each i-th iteration generates block B_i from the current realizing object $\overline{M_i} = M \setminus \cup_{j=1}^{i-1} M_j$, with a randomly determined direction $d_{i,1}^{AM}$ as the AM direction of B_i. The top-down strategy continues until the entire shape M is decomposed, as shown in Figure 5. By reversing the order of the decomposed blocks, we generate a feasible ASHM manufacturing sequence. section 4 details generating one desired block B_i in one top-down iteration. We encode all ASHM manufacturing constraints using a well-defined slab-based dynamic-directed graph, followed by a greedy node merging procedure to generate blocks. In section 5, we introduce a beam-guided search scheme to explore additional possibilities for ASHM direction selection to generate large number of candidate blocks, and select optimal

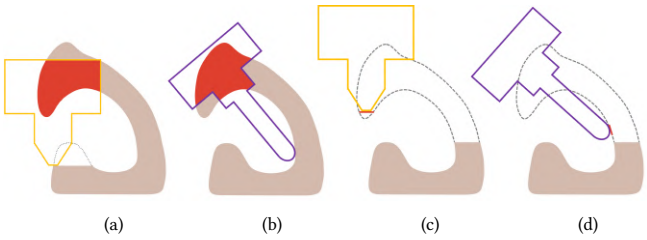

Fig. 6. Illustration of manufacturing constraints with four failure cases. (a) Additive accessibility constraint: collision between the print head and the realized part during AM. (b) Subtractive accessibility constraint: collision between the machining cutter and the model during SM. (c) Additive dependency constraint: without using support structures, a slicing slab can be printed only after its precedence slabs. (d) Subtractive dependency constraint: the machining cutter cannot carve over an in-existent 3D surface.

combination from them. For clarity of exposition, we explain the methodology for 2D illustrations. [5]

3.2 Manufacturing Constraints

As mentioned before, our current solution is based on support-free hybrid manufacturing from scratch using flat print slicing slabs and a 3+2 machining strategy, where two manufacturing collision-free related constraints (additive accessibility constraint and subtractive accessibility constraint), one manufacturing dependency constraint, and a self-support constraint would be the key manufacturing constraints to be considered during sequence planning.

Additive accessibility constraint. In the conventional 3-axis layered fabrication, collisions between the print head and the realized part aren't going to exist since the realized part is consistently below the current print slab. However, for the 5-axis additive process of our ASHM setting, different blocks may apply different print orientations, where we should avoid collisions between the print head and the realized part, see Figure 6(a). In this paper, such collision-free manufacturing constraint is formulated as additive accessibility, which is computed in subsection 4.2.

Subtractive accessibility constraint. Similar to additive accessibility, subtractive accessibility is used to guarantee collision-free between the machining cutter and the realized part during the subtractive manufacturing step of ASHM, see Figure 6(b). The subtractive process of ASHM corresponds to the fine-machining stage of the conventional CNC machining process, where a ball-end CNC cutter would further carve the external 3D surface to increase the surface quality by removing all staircase artifacts raised by additive layered fabrication. This constraint is computed in subsection 4.1.

Dependency constraint. This constraint is to formulate the dependency relationships between different manufacturing stages of ASHM, which means that a manufacturing operation cannot be applied without completing the precedence steps on which it relies, named *dependency constraint.* For additive manufacturing, a block can only be printed on a realized part, and a slicing slab can be printed only after some other slabs, shown in Figure 6(c). For subtractive manufacturing, it indicates that the machining cutter cannot carve over an in-existent 3D surface (Figure 6(d)).

Self-support constraint. Since support structures may damage the areas where have been machined, achieving self-supporting printing is necessary. Following [Wu et al. 2020a], we formulate the self-support constraint on each sampling point p of the target shape. A maximal self-supporting angle α_{max} is included to restrict the surface normal of all sampling points from the current print direction, $n_p \cdot d + sin(\alpha_{max}) \geq 0$, where n_p is the unit normal vector of p, d is the unit direction vector of print. We set α_{max} to 50°. This constraint would be applied in subsection 4.4.

4 CO-DECOMPOSITION METHOD

This section details the method to decompose B_i in i-th iteration (i is initialized as 1) from the realizing 3D object $\overline{M_i}$ (initialized as the input object M, $\overline{M_i} = M \setminus \cup_{j=1}^{i-1} M_j$) with a determined AM direction $d_{i,1}^{AM}$. Inspired by [Zhong et al. 2022], we apply an over-segmentation-then-merging strategy. With uniformly slicing $\overline{M_i}$ with flat planers vertical to an AM direction, the result of slicing slabs is taken as the over-segmented-small-scale blocks, which will be further merged into large-scale blocks with guaranteeing hybrid-fabricable for ASHM.

Our key idea is to encode all ASHM manufacturing constraints with a well-defined dynamic-directed graph, *hybrid block graph*, G_i^{ASM}, whose nodes are slicing slabs and edges encode ASHM constraints such as AM/SM tool accessibility, manufacturing dependency, etc. To build G_i^{ASM}, we need first to build a *subtractive block graph* G_i^{SM}, and a *additive block graph* G_i^{AM}. G_i^{SM} encodes the subtractive accessibility constraint to carve $\partial\overline{M_i}$ by SM from a group of potential SM directions (subsection 4.1). G_i^{AM} encodes the additive accessibility constraint, additive dependency constraint, and self-support constraint to print $\mho\overline{M_i}$ by AM (subsection 4.2). Then integrate G_i^{SM} and G_i^{AM} to the hybrid block graph G_i^{ASM} (subsection 4.3). Finally, we generate a large-scale block with a greedy node merging procedure from G_i^{ASM} (subsection 4.4).

4.1 Subtractive Block Graph

When segmenting B_i from the realizing object $\overline{M_i}$, it is crucial to determine whether an area is accessible of the object surface $\partial\overline{M_i}$ using a specific machining cutter direction and to identify the cause of the collision if it's inaccessible.

To gather this information on subtractive accessibility, we construct the subtractive block graph G_i^{SM}. In this graph, nodes represent the sampling surface points of $\partial\overline{M_i}$, and directed edges between nodes represent their obstructing relationship from specific SM directions. As shown in Figure 7(a), the purple frame indicates the machining cutter to carve point h along the vertical direction, where six points of $\{j, i, f, d, c, a\}$ obstruct the cutter. Hence, we build six directed edges from h to $\{j, i, f, d, c, a\}$. We associate a bit vector to each directed edge, whose vector length equals the number of sampling machining directions. The j-th bit indicates if the endpoint of the directed edge collides with the machining cutter when

[5] The pseudocode for the algorithm, along with the introduced concepts and mathematical symbols, can be found in the supplementary material.

carving the start point from the j-th machining direction. 0 means collision-free, while 1 indicates collision. In Figure 7(a), three sampling matching directions are evaluated ($\uparrow, \leftarrow, \rightarrow$). The bit vector $[1, 0, 0]$ of edge (h, i) means that point i collides with the cutter when carving point h with the vertical cutter direction ($\uparrow$); point i do not collide with the cutter when carving point h with the other two cutter direction ($\leftarrow, \rightarrow$).

In the real manufacturing, most 5-axis ASHM machines can only orient their print head and CNC cutter downwards at an oblique angle ranging from 0° to 90° [Dezaki et al. 2022]. Therefore, we uniformly sample potential SM cutter directions from the upper hemisphere of a Gaussian sphere, resulting in $\mathcal{D}^{SM} = \{d_1^{SM}, d_2^{SM}, ..., d_n^{SM}\}$ (n is 200 in our setting). The associated CNC cutter directions D_i^{SM} of the target B_i is a sub set of $\mathcal{D}^{SM}$.

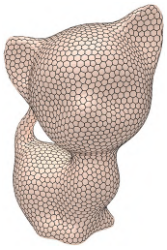

Subtractive Block Graph in Initialization. If it's the 1-st iteration, we employ Lloyd's Voronoi relaxation algorithm to achieve uniform sampling on ∂M. The resulting Voronoi sites are then taken as the surface sampling points $\mathcal{P} = \{p_1^{SM}, p_2^{SM}, ..., p_n^{SM}\}$, taken as graph nodes of G_1^{SM}. We individually attempt manufacturing every sampling point p_i using each subtractive direction d_i^{SM}. This is achieved by rotating the machining cutter in the direction d_i^{SM} to point p_i. If there is no collision, we define point p_i as accessible to the SM direction d_i^{SM}. Otherwise, we must determine which surface sampling points obstruct the point p_i. This can be done by checking if the sampling points lie within the cutter, as the points $\{j, i, f, d, c, a\}$ in Figure 7(a), which are inside the purple frame of the machining cutter to carve point h along the three directions ($\uparrow, \leftarrow, \rightarrow$). We build directed edges of G_1^{SM} by taking point p_i as the start node and the points obstructing p_i as the endpoints.

Further, we associate a bit vector for each node, which is the union of the bit vectors of the node's outgoing edges; for example, the bit vector of node h is $[1, 1, 1]$ since the three directions are inaccessible in Figure 7(a). For a bit vector where all the values at each position are 1, its corresponding surface sampling point is inaccessible to any sampling machining directions, called a subtractive inaccessible point (red nodes in Figure 7(a)). Otherwise, it is an accessible point. We use green nodes indicating surface sampling points that obstruct the inaccessible points. Note that we did not record the directed edges between two accessible nodes. This strategy can reduce memory consumption.

Subtractive Block Graph in Top-down Process. In the absence of iteration ($i \geq 2$), building G_i^{SM} from G_1^{SM} is relatively straightforward process. Considering the realizing shape ($\overline{M_i}$) to be decomposed. This can be done by first removing all nodes and related directed edges of G_1^{SM} which does not belong to $\overline{M_i}$, then updating the nodes' bit vectors. As shown in Figure 7(b), the inaccessible point "e" becomes accessible.

4.2 Additive Block Graph

Similar to subtractive block graph, we encode additive manufacturing constraints (additive accessibility, additive dependency and self-support constraints) into additive block graph G_i^{AM}. Note that

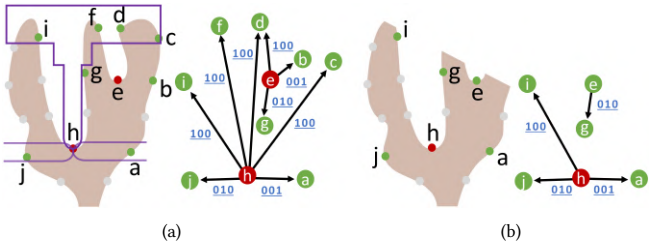

Fig. 7. Illustration of subtractive block graph G_i^{SM}. Three matching directions are evaluated ($\uparrow, \leftarrow, \rightarrow$). (a) For the input 3D object M, we start to uniformly sample points over the 3D surface of M (2D boundary in this illustration). The purple frame indicates the machining cutter to realizing point h along the three directions, collides with points $\{a, c, d, f, i, j\}$, encoded by the associated bit vector of directed edges. The directed graph shows the result subtractive manufacturing graph, where points h and e are inaccessible (red dots). (b) Build the subtractive block graph $G_i^{SM}, i \geq 2$ to decompose $\overline{M_i}$, where a sub-part of the top-right corner has been decomposed to a block in previous top-down iteration. The inaccessible point e is now accessible.

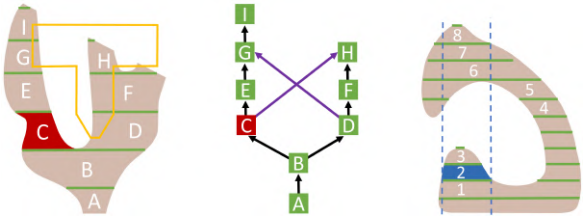

Fig. 8. (a) Illustration of additive block graph G_i^{AM}, whose nodes are slicing slabs on the left, with two types of edges, the dependency directed edges (black edges), and the collision directed edges (purple edges). The self-support slabs are illustrated with a green square, and the red squares indicate non-self-support slabs. (b) To speed up the collision detection between two slabs, we find that the collision can be determined in some specific cases without the time-consuming traversing process, taking slab 2 for an example: 1) slabs under slab 2 will never collide to slab 2 (slab 1); 2) slabs that depend on slab 2 will never collide to slab 2 slab 3; 3) for slabs that do not depend on slab 2, they will definitely collide to slab 2, if there are intersections in the 2D projection space along the print direction, such as slabs 6, 7, 8.

each G_i^{AM} only corresponds to one additive direction $d_{i,1}^{AM}$. From what we know, [Zhong et al. 2022] is the first work that builds a directed graph to represent the dependency relationships and the global collision constraints for the 3-axis additive manufacturing of the surface model.

We build our G_i^{AM} directly following the proposed *dependency OPP graph* of [Zhong et al. 2022] except for a minor difference (see an example in Figure 8(a)); that is, we extend nodes from slicing surface models to solid models, where each node of G_i^{AM} encodes a slicing slab of the realizing shape $\overline{M_i}$.

To build our additive block graph G_i^{AM}, we start by uniformly slicing $\overline{M_i}$ with flat planers vertical to $d_{i,1}^{AM}$. The result of slicing slabs is taken as the graph nodes of G_i^{AM}. Then build the *dependency directed edges*, if the horizontal distance between two adjacent slabs

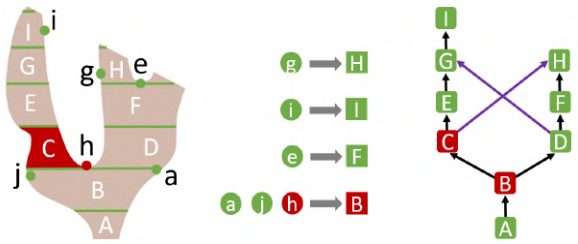

Fig. 9. Illustration of unified accessibility analysis to build G_i^{ASM}. (a) The sampling surface points and slicing slabs of G_i^{SM} and G_i^{AM}. (b) The many-to-one mapping relationship between the two graphs' nodes by the location of surface points. (c) G_i^{ASM} is constructed by labeling the subtractive inaccessible nodes in G_i^{AM}. There are two non-fabricable nodes, node B to be inaccessible for the SM process, and node C to be non-self-support. Nodes of G_i^{ASM} are visualized with rounded rectangles to indicate the integration of the two graphs' nodes, which are visualized by circular dots and rectangles with right corners separately.

(neighboring slicing slabs that are vertically adjacent (black edges in Figure 8(a))) is shorter than the AM path width (2 mm), we add a dependency directed edge of G_i^{AM} from the bottom slab to the top one. The dependency directed edges signify that the slab of the end node of the edge can only be printed after the slab of the start node of the edge has been printed. Printing a slab node is only possible once all the nodes it depends on have been printed. For the global collision constraint, we introduce another type of directed edge called *collision directed edges*. We generate a collision dependency edge between each node pair of G_i^{AM} if the end slab node collides with the print head while printing the slab of the start node. That is done by traversing the internal areas of each slab with the print head to determine whether other slabs collide with it while printing the slab. Note that we must always maintain G_i^{AM} as a Hasse diagram [Pemmaraju and Skiena 2003] by reducing redundant dependency edges.

We further associate a label for each node of G_i^{AM} to indicate whether it's self-support in $d_{i,1}^{AM}$ and a label for each slab node to indicate whether there is a collision with the ASHM machine's base planner while printing this slab. In addition, we propose a novel strategy to speed up further the collision detection between two slabs, shown in Figure 8(b).

4.3 Hybrid Block Graph

We further aim to integrate the AM and SM feasibility by integrating G_i^{AM} and G_i^{SM} into a new directed graph G_i^{ASM}, whose node encodes both the sampling points over the 3D surface of the SM graph, and the slicing slabs of the AM graph.

We first copy G_i^{SM} to G_i^{ASM}, then assign a new label for each node to indicate its current subtractive accessibility. The new label is computed from a many-to-one mapping between the nodes of the two graphs. As Figure 9(b) shows, each surface point of G_i^{SM} is mapped to its located slicing slab of G_i^{AM}. The node of G_i^{ASM} is labeled subtractive inaccessible if its related surface points are current subtractive inaccessible.

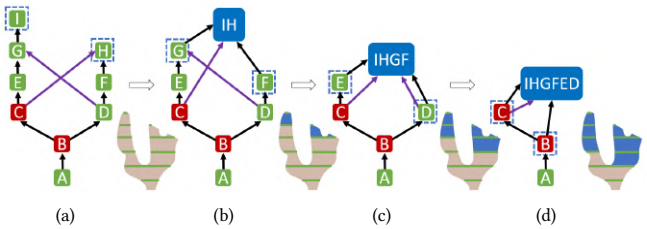

Fig. 10. An example of hybrid-fabricable block generation with three node merging iterations. The blue dashed box indicates the merging nodes in G_i^{ASM} to the block (the blue rounded rectangle), as the fabricable leaf nodes I and H for the first iteration (a to b). The merging process terminates while all nodes related to the block are not fabricable (d), such as nodes C and B.

4.4 Generating Hybrid-fabricable Block

This step aims to generate a block B_i from G_i^{ASM} with a greedy node merging procedure (Figure 10). Each leaf node of G_i^{ASM} can be taken as a block, if the leaf node is subtractive accessible, self-support and without collisions between the ASHM machine. All leaf nodes make up the initialized block of graph merging, which can be further enlarged by including other non-leaf nodes. The specific merging criteria are listed: 1) existing directed edges to the block's nodes; 2) subtractive accessible; 3) without destroying the self-support constraint of the enlarged block; 4) the enlarged block doesn't collide with the ASHM machine. The graph merging stops when no non-leaf nodes can be included in the block, resulting in the generated B_i as the combination of the merged nodes of slabs.

Suppose the associated M's sub-part of B_i is $M_{i,1}$. With the current generated block B_i, we attempt to enlarge B_i further by switching to other additive directions, referring as *block enlarging procedure*. To do that, we first get a new realizing object $\overline{M_{i,2}} = \overline{M_i} \setminus M_{i,1}$. Then build a new additive block graph $G_{i,2}^{AM}$ of $\overline{M_{i,2}}$ with another randomly generated AM direction $d_{i,2}^{AM}$. After that build the hybrid block graph $G_{i,2}^{ASM}$ by integrating $G_{i,2}^{AM}$ and G_i^{SM}. Finally, we apply the greedy node merging procedure once again from $G_{i,2}^{ASM}$, resulting in block is $B_{i,2}$. If $B_{i,2}$ is not empty, we combine $B_{i,2}$ and B_i to one single block, and continue the block enlarging procedure until the newly generated block is empty. Note that if the final resulting block B_i is really enlarged by applying the *block enlarging procedure*, multiple AM directions are associated to B_i. See the blue block of the *Coral* model in Figure 18.

5 BEAM-GUIDED OPTIMIZATION

Our main motivation for applying the beam-guided strategy for the VASCO problem is the observation that the choice of different AM directions for each block substantially impacts the length of the sequence planning. This section provides a detailed description of the proposed beam-guided strategy, which aims to explore additional possibilities for ASHM direction selection. Beam search is a heuristic search algorithm to strike a trade-off between efficiency and solution quality. In each iteration, we generate plenty of candidate blocks with different AM direction using the method of section 4. The core steps lie in 1) generating multiple candidate solutions (subsection 5.1); 2) scoring the candidate's solution, then

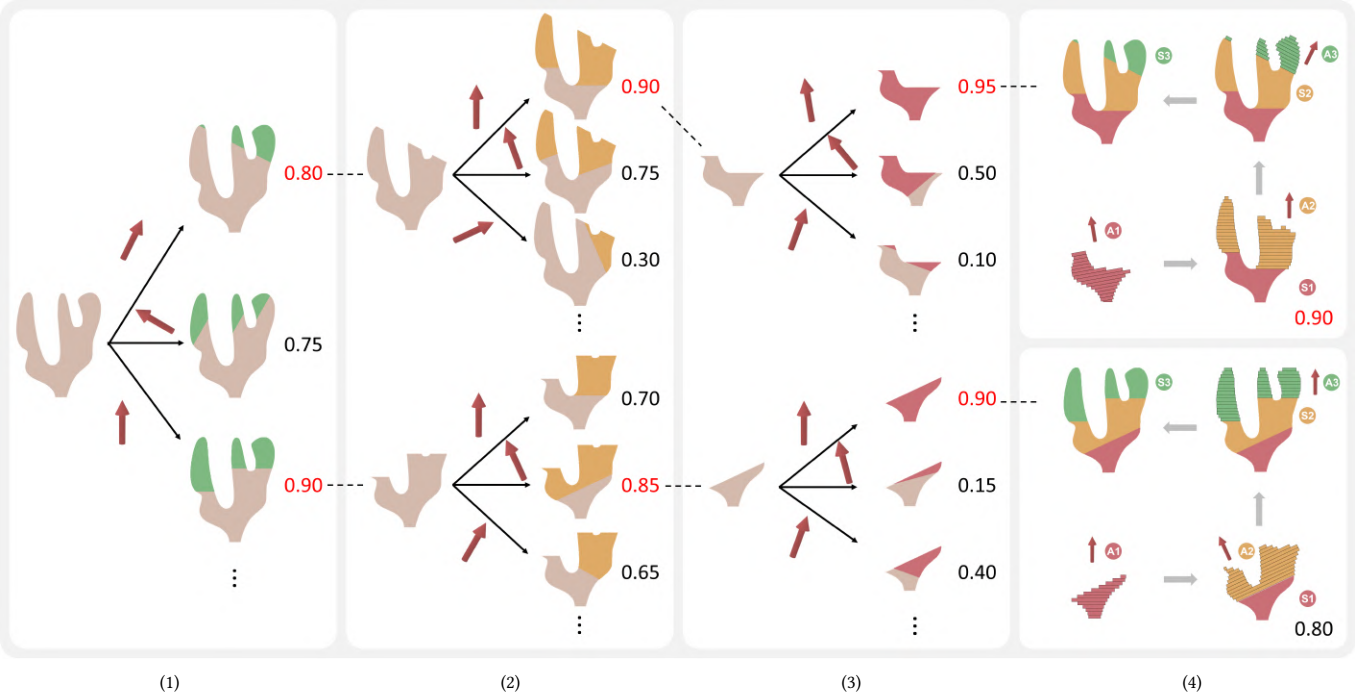

Fig. 11. We have devised a beam-guided search approach to expand the possibilities for ASHM direction selection to improve upon the local-optimum results obtained from a simple greedy scheme. This figure demonstrates the input *coral* model evolution for a complete decomposition of the beam-guided optimization with three beam-guided iterations (1-2-3). Selected candidates are marked with a box during each iteration. We set the beam width $W_{beam} = 2$ and sample $D_{Dir}^{AM} = 10$ AM directions (deep red arrows). The numbers marked in the figure represent the block evaluation value $f_{priority}(B)$. (4) shows the optimal ASHM manufacturing sequence (the top one). For easy visualization, we suppose not applying the block enlarging procedure described in subsection 4.4.

selecting the optimal W_{Beam} (W_{Beam} is set 8) (subsection 5.2); 3) termination condition (subsection 5.3). Figure 11 demonstrates the model evolution for a complete decomposition.

5.1 Generating candidate solutions

In the preprocessing stage of beam search, we uniformly sample N_{Dir}^{AM} potential AM print head directions from the upper hemisphere of a Gaussian sphere, resulting in $\mathcal{D}^{AM} = \{d_1^{AM}, d_2^{AM}, ..., d_n^{AM}\}$ (we generate 100 directions in our implementation). Then we call the method discussed in section 4 with our input 3D object M and each sampling AM direction as input to the block co-decomposition method. The co-decomposition method will output N_{Dir}^{AM} block decompositions. During the iterative process, we calculate each selected candidate solution's resulting 3D object by removing the previously generated blocks. We then call the method described in section 4 for further processing.

5.2 Hybrid-fabricable block evaluation

This subsection proposes an evaluation function to select W_{Beam} best blocks from $N_{Dir} \times W_{Beam}$ candidate blocks during each beam iteration. The evaluation function is to rate each candidate block, where blocks with high evaluation scores should be beneficial for,

- minimizing the length of sequence planning: 1) each block's size should be as large as possible; 2) set higher priority to the surface points that obstruct the inaccessible points of G_1^{SM} in the top-down decomposition process; (note that these two criteria are heuristics and do not guarantee their effectiveness);
- manufacturing efficiency: 3) minimize the number of connected components of each block, which aims to improve the toolpath continuity by reducing the amount of transfer movement of the print head in AM;
- manufacturing stability: 4) minimize the change in print directions of two sequential blocks to avoid applying the next AM process on a platform with staircases raised from the previous block; 5) structure soundness to avoid generating fragile blocks, i.e., "bridges" (elongated channel connecting two larger parts) and "thin fins" (plate-like structures, such as airfoil), where we should avoid decomposing such fragile structures of M into different blocks; 6) desired pyramid-like shapes of blocks to improve the additive manufacturing stability.

Figure 12 illustrates the effectiveness of each criterion by a single-variable experiment. It's easy to see that the first two criteria are really beneficial for minimizing the number of blocks. We attempt the further analyze the two criteria with an ablation study in Figure 13. While the other four criteria would conflict with that goal.

Fig. 12. Single variable comparison of each evaluation criterion, where we evaluate the generated blocks with only considering one of the six criteria. From left to right, this figure shows the decomposition results of (1) "Size of block"; (2) "Surface point priority"; (3) "Block connectivity"; (4) "Changing in print directions"; (5) "Structure soundness"; (6) "Pyramid-like shapes". The number of resulting blocks is indicated in the figure.

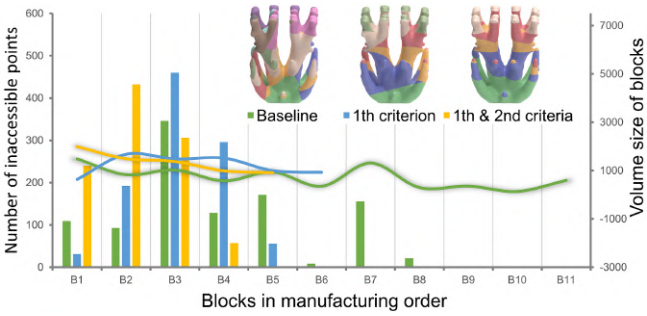

Fig. 13. Criteria analysis with an ablation study, with three block decomposition results generated by 1) a baseline method, in which we randomly select blocks during each beam search iteration (green bar and line charts); 2) only take the "size of block" criterion as the block evaluation function (blue bar and line charts); 3) take the "size of block" and "surface point priority" criteria as the block evaluation function (yellow bar and line charts). The three methods produce 11, 6, and 5 blocks, separately. The bar chart illustrates how many inaccessible nodes of G_1^{SM} would be realized within each block. The line chart illustrates the size of each block.

We propose a weighted evaluation function to sum up them:

$$F(B) = \sum w_k f_k(B), k \in [1, 2, ..., 6] \tag{2}$$

where w_k is chosen to trade-off between different criteria, and each criterion term is normalized to be between zero and one. We set $w_1 = w_2 = 0.4, w_k = 0.05, k \in [3, 4, 5, 6]$. This subsection will detail the first two criteria and demonstrate their impact, while the last four are formulated in the supplementary material.

Size of block. Making block as large as possible is a straightforward heuristic to minimize the number of "AM-then-SM" steps. Compared to small blocks, bigger blocks gives a better chance of minimizing the total number of blocks. Since we produce the block decomposition based on slicing slabs, we perform an approximation method to evaluate the size of a block B efficiently, where we sum up the length of its slabs' bottom contours:

$$f_{size}(B) = \sum Length(s_B), s_B \in S_B \tag{3}$$

where S_B indicates the set of all slabs in B, s_B is one slab of S_B, and $Length(s_B)$ is the length of the bottom contour of s_B.

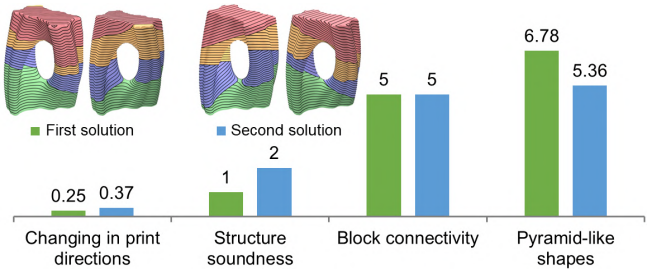

Fig. 14. Multiple decomposition results from the beam search, with the identical number of blocks. For the model *Julia vase*, we show two solutions with identical 4 blocks. This figure shows the front and back views of the two solutions. The bar chart visualizes four measurement values following the last four criteria, in which a smaller value means better. The first solution is with better *changing in print directions* and *structure soundness*, and the second solution is with better *pyramid-like shapes*.

Surface point priority. As told in section 1, during the top-down decomposition process, the generated blocks should include as many as possible regions that would obscure the inaccessible regions of G_1^{SM}. We suppose to set higher priority to the surface points that obstruct the inaccessible points of G_1^{SM}. That can be done by computing a "priority value" of each surface point, which is the number of inaccessible points that are obscured by the surface point in all sampling directions. We exploit this measure as an evaluation function:

$$f_{priority}(B) = \sum Priority(s_B), s_B \in S_B \tag{4}$$

where S_B indicates the set of all slabs in B, s_B is one slab of S_B, $Priority(s_B)$ is the total priority value of all surface points of s_B. Note that our evaluation function can be modified easily according to the demands in the specific manufacturing scenarios.

5.3 Final selection of hybrid manufacturing sequence

The beam-guided strategy terminates until decompose the whole M. Once the beam search is terminated, it may result in multiple hybrid manufacturing sequences with the identical account of blocks. We propose to reuse the last four criteria to evaluate the produced blocks of each generated manufacturing sequence. Then select the sequence with the best evaluation value, which is with the minimized number of "AM-then-SM" steps together with the best manufacturing efficiency and stability (Figure 14).

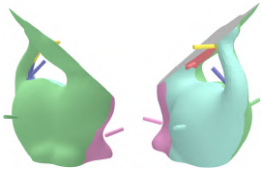

We employ the 3+2 machining strategy during the CNC machining stage. Specifically, we utilize a graph-cut-based method described in [Zhao et al. 2018] to decompose the external surface of each block into a series of height fields. The inset figure illustrates this process. As depicted, the first block of the kitten model is decomposed into six height-field patches, each distinguished by a different color. Subsequently, we perform subtractive machining with six CNC directions, denoted by small cylinders, on these patches.

	Shape		Initial			Process		Results		
Model	H	R_s	#S	$\#P_i$	R_p	$\#B_C$	$\#I$	$\#B$	$\#O$	#C
Coral	61	3.82	11672	279	0.02	608	3	3	3	15
Bunny	105	1.07	5550	48	0.01	492	3	3	3	5
Kitten	85	1.04	10342	4	0.00	341	2	2	2	2
Hand	140	2.29	9209	772	0.08	676	3	3	3	11
CornerHolder	53	3.68	6611	577	0.09	688	3	3	3	5
BottleOpener	53	4.69	6073	444	0.07	1072	4	4	7	5
Julia vase	80	4.56	8847	548	0.06	756	4	4	4	5
TPMS	56	12.6	14907	349	0.02	928	4	4	8	21
Shelf	86	6.68	9370	327	0.03	1560	9	9	10	13
Impeller	21	1.98	9810	0	0	69	1	1	1	1
Four-way pipe	40	1.49	6480	660	0.10	964	4	4	4	4
Exhaust	40	0.79	8059	1427	0.18	1239	6	6	6	13

Table 1. Statistics of the shapes shown in the paper. H is the height (mm) of the model. R_s is the surface-area-to-volume ratio. #S is the number of sample points on the shape surface. $\#P_i$ is the number of inaccessible points. R_p is the ratio of inaccessible points to sample points. $\#B_C$ is the total candidate blocks of the beam search. $\#I$ indicates the number of beam search iterations. $\#B$ is the number of resulting blocks in the final selected decomposition. $\#O$ is the sum of additive orientation in the blocks. #C is the number of connected components.

	Initial	Process				
Model	G_1^{SM}	G_i^{SM}	G_i^{AM}	G_i^{ASM}	EV	$T(min)$
Coral	38	35	11	9	175	4.5
Bunny	4	6	9	3	57	1.3
Kitten	8	7	6	2	84	1.7
Hand	49	22	17	10	148	4.1
CornerHolder	34	11	12	5	87	2.5
BottleOpener	23	28	33	18	126	3.8
Julia vase	38	36	16	8	103	3.4
TPMS	60	143	71	47	484	13.4
Shelf	34	115	44	27	220	7.3
Impeller	6	1	1	1	29	0.6
Four-way pipe	44	20	11	4	59	2.3
Exhaust	94	84	25	13	132	5.8

Table 2. This table reports the running times (in seconds) for building initialized subtractive block graph (G_1^{SM}), subtractive block graph during the top-down decomposition (G_i^{SM}), additive block graph (G_i^{AM}), the block generation by merging the unified manufacturing graph (G_i^{ASM}), and the block evaluation time (EV). T is the total running time (in minutes).

6 RESULTS AND DISCUSSIONS

This section demonstrates the ASHM sequence planning results of 3D models with varying degrees of geometric complexity and the physical evaluation results. We also evaluate the performance of our VASCO algorithm in terms of different parameter settings. Discussion is proposed on object manufacturability, weight assignment, and the validation of the algorithm scalability.

6.1 Implementation and Parameters

The implementation of our algorithm was carried out in C++, utilizing a PC equipped with an Intel Core i7-11700 CPU operating at 2.5 GHz and 16GB of memory. In the subtractive accessibility analysis, we sampled 200 subtractive directions, while for generating G_i^{AM}, we utilized 100 additive directions. The self-support angle threshold was set to 50°, and a slice layer thickness of 2.0 mm was employed. Further details regarding the tool parameters can be found in the supplementary material. To simulate the VASCO results, we utilized the [SIEMENS] NX 2206 software, utilizing the "Multi Axis Deposition" and "Manufacturing" modules. For each block, additive and subtractive paths were generated based on the specified directions, with collision detection being performed to ensure collision-free operations. Physical evaluation was conducted by transforming a desktop 5-axis CNC machine into a desktop ASHM machine. A video demonstrating the manufacturing process, which consistently remained collision-free, accompanies this paper.

6.2 Decomposition results

We demonstrate the decomposition results for 11 freeform models in Figure 15, and also list the statistic data in Table 1 and running time in Table 2, to examine the beam-guided top-down decomposition algorithm performance.

Generally, the number of blocks correlates with the shape complexity and distribution of inaccessible regions. Shapes with a high surface-area-to-volume ratio (*Shelf*) or numerous inaccessible points (*Julia vase*) require longer sequences. Smaller shapes with concavities face (*Bottle Opener*) increased inaccessibility due to potential cutter-workpiece collisions. Three models exhibit multiple additive manufacturing directions in one block, as seen in the green block of the *Shelf* model and the blue and red blocks of the *TPMS* model in Figure 15. Our algorithm generates multiple candidate decompositions (Figure 14), providing experts with more options. This flexibility enhances the ASHM process by accommodating diverse manufacturing requirements.

Performance. Regarding to time consumption, our algorithm takes 6 minutes on average for an arbitrary target shape, shown in Table 2. The most time-consuming procedure is to build the additive block graph (G_i^{AM}), and the block generation process from G_i^{ASM}. The two steps would be applied many times during the beam search. Compared with the running time of the initialized subtractive accessibility analysis (G_1^{SM}), our algorithm is much more efficient in building each additive block graph, which takes only 0.02 seconds on average.

Cutter sizes. For a fixed-size input 3D model, it is easy to understand that the size of the cutter can influence the size and distribution of inaccessible regions. In a scenario where a model has a larger

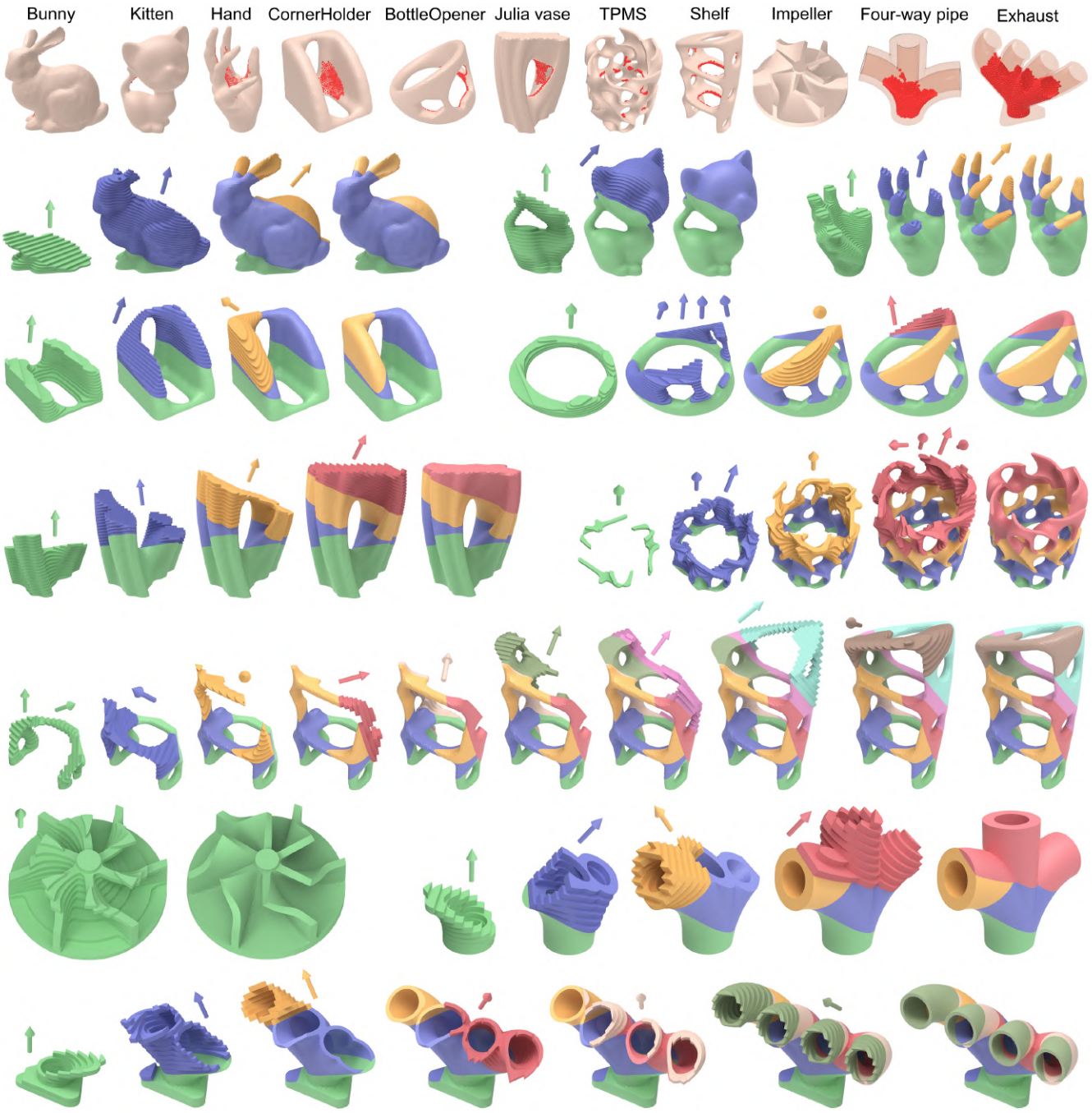

Fig. 15. Results gallery of ASHM sequence planning results generated by our beam-guided top-down decomposition method. The models are arranged in the order of *Bunny, Kitten, Hand, Corner Holder, Bottle Opener, Julia vase, TPMS, Shelf, Impeller, Four-way pipe, Exhaust*. The top row illustrates the inaccessible regions of each model, represented by red dots, which the machining cutter cannot reach. This assumption is made under the condition that the entire model has been additively manufactured. The subsequent rows visualize the ASHM sequence for each model from left to right, showcasing the staircase formed by the arrangement of slabs in AM process. The smoothing of high-quality surfaces produced by the subtractive process is also visualized. The arrows indicate the additive manufacturing (AM) directions for the hybrid-fabricable blocks. Note that we apply a larger inter-layer spacing of AM slabs for each visualization.

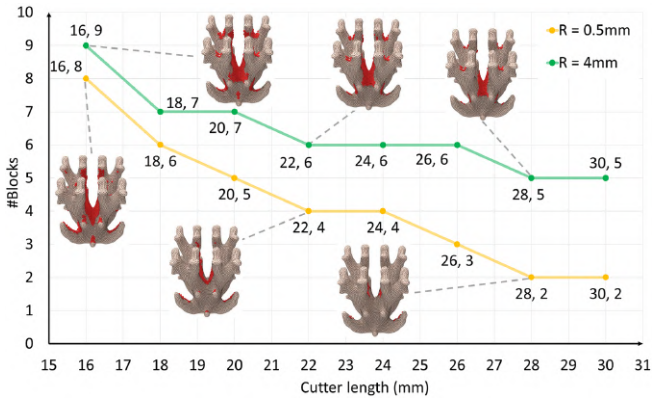

Fig. 16. Illustration of the relationship between the number of blocks generated by our method (vertical axis) and the cutter length (horizontal axis), with the *Coral* model. Two curves are depicted: the green curve represents the results obtained with a cutter with a radius of 4 mm, while the yellow curve corresponds to a cutter with a radius of 0.5 mm. Red points highlight inaccessible regions of partial models under certain parameter settings.

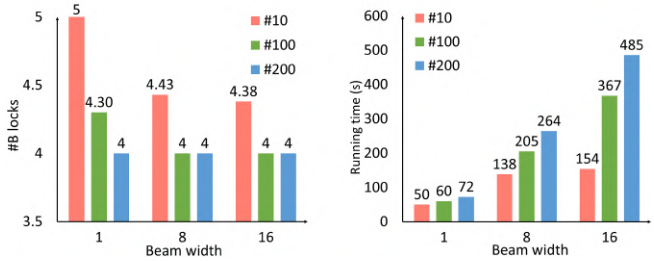

Fig. 17. With the *Julia vase* model, we validated our beam-guided top-down decomposition algorithm's performance under different combinations of parameters, the beam width W_{Beam}, and the number of sampling AM directions N_{Dir}^{AM}. For each bar, we randomly choose the directions and take the average of 10 tests. The horizontal axis in both the left and right graphs represents different values of beam width $W_{Beam} \in \{1, 8, 16\}$. The vertical axis in the left graph represents the number of output blocks, while the vertical axis in the right graph represents the runtime of our algorithm. The bar chart uses red, green, and blue colors to indicate three different parameter values $N_{Dir}^{AM} \in \{10, 100, 200\}$.

area of inaccessible regions, it is expected to have a higher probability, which corresponds to a longer ASHM sequence length. As shown in Figure 16, we experimented with validating whether our algorithm could produce the expected results in this scenario. At first, we can see that a longer cutter indeed reduced inaccessible regions' area of the *Coral* model, and a "fatter" cutter ($R = 4$ mm) indeed produced larger inaccessible regions compared with a "thinner" cutter ($R = 0.5$ mm), where a "fatter" cutter is hard to access those concave areas of the *Coral* model. Two curves in Figure 16 visualize our method's block decomposition results. The experimental results demonstrate that our algorithm can produce highly expected block decompositions. Specifically, fewer blocks are generated as the cutter becomes finer and longer.

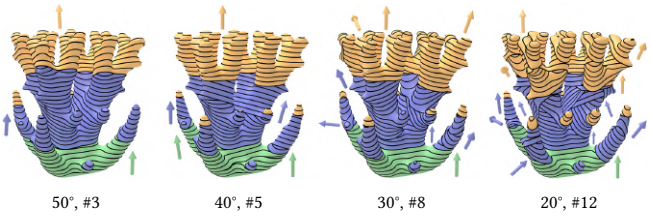

Fig. 18. For model *Coral*, this figure presents the results of our algorithm under the different parameters of maximal self-supporting angle $\alpha_{max} = \{50°, 40°, 30°, 20°\}$. Our algorithm achieves the same number of blocks regardless of the parameter α_{max}, three blocks indicated with colors of green, blue, and yellow. However, as the maximal self-supporting angle α_{max} decreases, more printing directions are required for additive manufacturing of the three blocks. The values of α_{max} and the number of AM directions are labeled in the figure. The deep red arrows in the graph indicate the AM directions.

Beam width and sampling AM directions. Our algorithm employs a beam-guided searching strategy, which offers a key advantage of striking a balance between algorithm efficiency and performance. In our algorithm, the parameter beam width W_{Beam} and the number of sampling AM directions N_{Dir}^{AM} control this balance. Generally, larger values of W_{Beam} and N_{Dir}^{AM} result in longer computation time but yield better results (a shorter ASHM sequence). Figure 17 showcases the results of applying different parameters W_{Beam} and N_{Dir}^{AM} values to a given *Julia vase* model, including the number of decomposed blocks obtained and the corresponding runtime of the algorithm.

Maximal self-supporting angle. In the VASCO formulation, we assume self-support in additive manufacturing of ASHM, where the parameter of maximal self-supporting angle α_{max} is used to identify the self-support constraint. Generally, a larger self-supporting slope angle imposes fewer constraints on the algorithm's freedom. Figure 18 illustrates the block decomposition results of model *Coral* with different parameters of α_{max}. It is observed that the algorithm achieves the same number of block decomposition. However, as the maximal self-supporting angle α_{max} decreases, more directions are required for the AM process of the three blocks. The reason for such results lies in the terminal conditions defined in subsection 4.4, where we further enlarge the generated block by switching to other additive directions while the node merging procedure from the hybrid block graph G_i^{ASM}.

6.3 Physical evaluation

Due to the limited availability of equipment for ASHM, particularly the high costs associated with ASHM equipment for metal materials and part processing, the research on essential issues from the field of computer graphics is significantly hindered. Therefore, we choose to modify a typical desktop 5-axis subtractive machine tool, which costs around $7K US dollars and less than 5% of the commonly used metal additive-subtractive equipment. Although this approach only allows the processing of plastic materials such as PLA, it does not affect the generality of graphical issues in ASHM, such as segmentation and path planning. We believe that, motivated by our modification approach, more researchers in the graphics field can

Fig. 19. Our ASHM machine was modified from a CNC machine (YORNEW Benchtop 5 Axis CNC MX220). The accessories of the additive module are installed above the machine (left). The additive extrusion module is connected with the machine spindle in parallel (upper right). The lower right corner demonstrates the additive process and subtractive process.

actively engage in relevant research on additive-subtractive hybrid manufacturing.

Specifically, we converted a desktop 5-axis subtractive machine (YORNEW Benchtop 5 Axis CNC MX220) into a simple 5-axis hybrid machine by adding an external additive extruder parallel to the tool spindle (see Figure 19 upper right). The 5-axis subtractive machine is composed of 3 linear movement axis and 2 rotational axes (B,C) around Y and Z axis. The travel distances of the X, Y, and Z axes of the five-axis machine are 220 $mm \times 120$ $mm \times 200$ mm. The travel ranges of the B and C axes are $+10^\circ$ to -120° and 360°, respectively. The repeatability accuracy of linear motion is 0.01 mm, and the rotation axis has a resolution of $12''$.

The key challenge is to enable the 5-axis subtractive machine to recognize and control the movements of the extruder, determine its position, and avoid collisions. We modify the circuit hardware (see Figure 19 left) and build a digital counterpart of the extruder in the simulation software. The external additive extruder is instructed by the controller of the 5-axis subtractive machine through G-code command. We use the user-defined-command M70/M71 to control the open and close of the extruder.

During the ASHM process, to maximize the usable workspace and avoid collisions, we manually remove the cutting tools used for subtractive operations during the additive phase. Since the tools have fixed positions for installation, the time required for removal and reinstallation is short, and no additional positioning calibration is needed. However, the CNC system employed in this approach only supports open/close operations for controlling the extruder. Consequently, we cannot perform retraction by reversing the extruder, resulting in significant stringing during idle travel and poor surface quality in the additive process. Nevertheless, these issues do not affect the final machining results, as the defects can be easily removed during subsequent subtractive steps. This aspect highlights the value of additive-subtractive hybrid manufacturing.

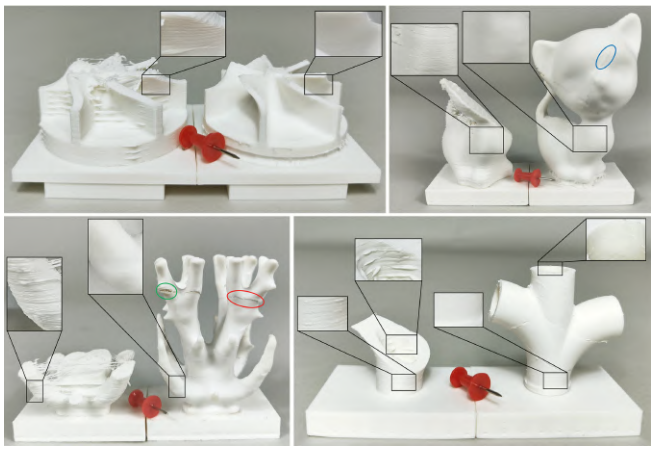

Fig. 20. The Impeller (1 block), Kitten (2 blocks), Coral (3 blocks) and Four-way pipe (4 blocks) were fabricated using our ASHM machine. Each model demonstrates the fabrication result (left) of the first block with a purely additive process and the result (right) after the whole ASHM process. Our approach owns higher surface quality compared to pure additive manufacturing. The Four-way pipe model improve the quality of both the outer surface and the inner channel. However, some defects still exist (blue, green, and red circles, which are mainly caused by our imperfect equipment and subtractive path planning.)

For the fabrication, we utilize Unigraphics-NX 2206 [SIEMENS] to produce both additive and subtractive tool paths. For AM, we employ the contour-parallel path, setting the in-fill rate to 30%, the tool path width to 0.5 mm, and the layer thickness to 0.2 mm. In the subtractive manufacturing stage, 3 + 2 machining strategy is adopted: the outer surface of each block is first segmented by [Herholz et al. 2015]'s methods to generate a set of machinable *height-field patches*; then generate an *areamilling* tool path for each height-field patch. We set the non-steep cutting path to *follow the perimeter* and the steep cutting path to *one-way deep machining*. The speed of main-shaft is set to 1500 rpm.

We show some fabrication results in Figure 20. The results demonstrate that our VASCO method can successfully achieve hybrid manufacturing of complex 3D objects[6]. The latter three models cannot be realized through a single "AM-then-SM" ASHM process. In the meantime, compared to pure additive manufacturing, our approach yields higher dimensional accuracy and better surface quality, effectively addressing the issues such as staircase defects.

In Figure 20, the seamline artifacts on the model surface appear on the boundaries. 1) Between blocks: the green circle highlights a small and thin area where multi-layers of printing path are highly concentrated in, causing the material to collapse; the red circle shows a seam line that is due to a slight misalignment during the reinstallation of the rotary-axis part in the modification process. 2) Within a block: the *height-field patches* are fabricated in different machining cutter directions (blue circle), which is mainly raised by the imperfect equipment setup and the generated tool path without considering the positioning compensation that may be necessary.

[6]Please refer to our supplementary video for the in-action demonstration of the actual manufacturing process.

Note that due to the constraints imposed by our current equipment's manufacturing space (about 60mm × 60mm × 90mm), we are unable to fabricate large-scale models, such as the Exhaust model (76mm length).

6.4 Discussion and Limitations

The VASCO problem is formulated from the geometric point of view. In the practical manufacturing process, more physical considerations must be carefully treated in the post-processing.

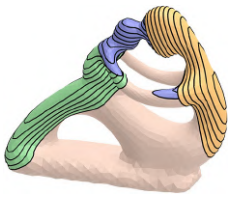

Object Manufacturability. The inset figure shows a failure case of the *fertility* model. Our algorithm failed to find a feasible solution with the default parameters. The reason is that the self-support and accessibility constraints cannot be simultaneously satisfied within the searched sampled directions. In the *fertility* model, if we consider the base pink area as the shape $\overline{M}$ that is realized within a single iteration of the beam-guided top-down process, then for every sampling additive direction used to realize $\overline{M}$, it is impossible to decompose any block from the resulting graphs G_i^{ASM}. In other words, all the leaf nodes in these G_i^{ASM} graphs are not fabricable. As a consequence, the beam search gets stalled. However, no solution found does not necessarily imply that this model is ASHM infeasible, as our VASCO algorithm cannot enumerate all printing directions, and the exploration of the search space is always limited by the search cost.

Weight assignment. Another issue is the weight assignment in the evaluation of the block candidate. In most cases, the default settings ($w_1 = w_2 = 0.4, w_k = 0.05, k \in [3, 4, 5, 6]$) produce nice results, but it is not guaranteed that this set of weights works universally regarding the target shapes and fabrication parameters. We believe involving learning-based techniques [Gao et al. 2021; Wu et al. 2020b] would help with the scoring strategy.

Object orientation. Another limitation of our current solution is that it does not take into consideration the object's inherent orientation, which is assumed to be provided by the user. We believe that different inherent orientations can result in distinct inaccessible regions for the ASHM tools. Therefore, incorporating orientation information may potentially lead to further reductions in the ASHM sequence length. We intend to explore this aspect in future research, and we believe that a learning-based approach holds promise to address this issue.

Algorithm scalability . To validate the algorithm's scalability, we conducted tests using lattice models of different scales in Figure 21. The bottleneck in our algorithm is building the subtractive block graph. Both the number of inaccessible points and surface sampling points for building the subtractive block graph G_1^{SM} directly affect the number of edges of G_1^{SM} and thus determine the scale of the graph. The three lattice models separately have 10844, 36497, and 92977 surface sampling points. Since the 30 mm^3 model owns a small size and simple geometry structure, almost all of these sampling points are accessible to the machining cutter. Therefore, it only takes

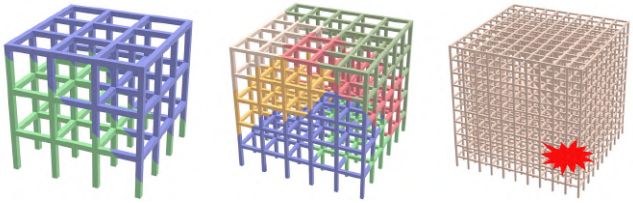

Fig. 21. An example of decomposing a lattice structure for ASHM sequence planning generated by our algorithm. The lattice models are constructed by Boolean operations on cube structures of different edge lengths. Each cube frame in the lattice mode has a consistent thickness $1.2mm$, and the distance between adjacent cube frames is also consistent, as $10mm$. From left to right, the lattice models have 3×3, 5×5, and 10×10 lattice cells, with corresponding dimensions of $30\times30\times30$ mm^3 , $50\times50\times50$ mm^3, and $100\times100\times100$ mm^3. Our algorithm successfully performs block decomposition for the first two models, resulting in 2 and 6 blocks. However, due to memory explosion, it cannot achieve segmentation for the last model.

92MB of memory and 9 seconds to build G_1^{SM}. In contrast, the other two models own much more complex structures and large sizes, causing many inaccessible points. The 50 mm^3 model needs 6.2GB memory and 18.6 minutes to build the graph. 50 mm^3 model is a failure case; it exceeds the memory limit of the computer (16GB). Our algorithm can solve the most commonly used models, but for this extremely complex model, more intelligent algorithms must be designed to solve the memory explosion problem. A possible solution is to dynamically generate the subtractive block graph, while the difficulty is how to properly pick the local edges, which we think is an interesting future work.

7 CONCLUSION AND FUTURE WORK

This paper introduces a novel computational framework aimed at addressing the sequence planning problem in additive/subtractive hybrid manufacturing (ASHM), which involves interleaved additive and subtractive processing. We propose a formulation called the "Volume-And-Surface-CO-decomposition, VASCO" problem, which aims to minimize the number of transitions between additive and subtractive processes while considering dynamic accessibility and manufacturing dependency constraints. Central to our approach is the concept of block, which combines printing volume and finishing surface properties, along with dynamic directed graphs that integrate the slabs of the block and the aforementioned constraints. To solve the VASCO problem, we present a beam-guided top-down block decomposition algorithm. Notably, our method surpasses previous approaches by being applicable to general sequence planning scenarios, without imposing restrictions on target shapes, hybrid sequence cycles, or manufacturing degrees of freedom.

Other manufacturing options can be taken into account to extend the VASCO formulation, 1) incorporating over/under-cut or over/under-fill manufacturing strategies [Harabin and Behandish 2022]; 2) considering simultaneously additive and subtractive manufacturing, where the print head and CNC cutter are working at the same time; 3) taking adaptive direction sampling method to build the subtractive and additive block graphs as some directions play more important roles; 4) considering volumetric subtractive

manufacturing to allow carving external volume while repairing deformed parts. These options may be included in our proposed algorithm by extension the formulation of block, the unified direction graph to encode more manufacturing constraints and include more criteria in our evaluation functions.

Hybrid manufacturing-oriented design can be further explored by combining our sequence planning method with space-time topology optimization [Wang et al. 2020]. Moreover, the feasibility study of an arbitrary given shape for ASHM is still an open problem. A reliable method that determines the feasibility of the target shape would greatly benefit shape optimization and practical CAM. Our VASCO algorithm produces an optimized solution for ASHM, and returns if no feasible solution is found. But it is just a necessary condition for the feasibility study. We would like to further dig into this problem.

REFERENCES

T. Alderighi, L. Malomo, T. Auzinger, B. Bickel, P. Cignoni, and N. Pietroni. 2022. State of the Art in Computational Mould Design. *Computer Graphics Forum* 41, 6 (aug 2022), 435–452. https://doi.org/10.1111/cgf.14581

Thomas Alderighi, Luigi Malomo, Bernd Bickel, Paolo Cignoni, and Nico Pietroni. 2021. Volume decomposition for two-piece rigid casting. *ACM Transactions on Graphics (TOG)* 40, 6 (2021), 1–14.

Thomas Alderighi, Luigi Malomo, Daniela Giorgi, Bernd Bickel, Paolo Cignoni, and Nico Pietroni. 2019. Volume-aware design of composite molds. *ACM Transactions on Graphics* (2019).

Thomas Alderighi, Luigi Malomo, Daniela Giorgi, Nico Pietroni, Bernd Bickel, and Paolo Cignoni. 2018. Metamolds: computational design of silicone molds. *ACM Transactions on Graphics* 37, 4 (aug 2018), 1–13. https://doi.org/10.1145/3197517.3201381

Chrystiano Araújo, Daniela Cabiddu, Marco Attene, Marco Livesu, Nicholas Vining, and Alla Sheffer. 2019. Surface2Volume: surface segmentation conforming assemblable volumetric partition. *ACM Transactions on Graphics* 38, 4 (aug 2019), 1–16. https://doi.org/10.1145/3306346.3323004

Michael Bartoň, Michal Bizzarri, Florian Rist, Oleksii Sliusarenko, and Helmut Pottmann. 2021. Geometry and tool motion planning for curvature adapted CNC machining. *ACM Transactions on Graphics* 40, 4 (aug 2021), 1–16. https://doi.org/10.1145/3450626.3459837

Morad Behandish, Saigopal Nelaturi, and Johan de Kleer. 2018. Automated process planning for hybrid manufacturing. *Computer-Aided Design* 102 (sep 2018), 115–127. https://doi.org/10.1016/j.cad.2018.04.022

Bernd Bickel, Paolo Cignoni, Luigi Malomo, and Nico Pietroni. 2018. State of the Art on Stylized Fabrication. *Computer Graphics Forum* 37, 6 (feb 2018), 325–342. https://doi.org/10.1111/cgf.13327

Li Chen, Tak Yu Lau, and Kai Tang. 2020. Manufacturability analysis and process planning for additive and subtractive hybrid manufacturing of Quasi-rotational parts with columnar features. *Computer-Aided Design* 118 (jan 2020), 102759. https://doi.org/10.1016/j.cad.2019.102759

Li Chen, Ke Xu, and Kai Tang. 2018b. Optimized sequence planning for multi-axis hybrid machining of complex geometries. *Computers & Graphics* 70 (feb 2018), 176–187. https://doi.org/10.1016/j.cag.2017.07.018

Niechen Chen and Matthew Frank. 2019. Process planning for hybrid additive and subtractive manufacturing to integrate machining and directed energy deposition. *Procedia Manufacturing* 34 (2019), 205–213. https://doi.org/10.1016/j.promfg.2019.06.140

Rulin Chen, Ziqi Wang, Peng Song, and Bernd Bickel. 2022. Computational design of high-level interlocking puzzles. *ACM Transactions on Graphics* 41, 4 (jul 2022), 1–15. https://doi.org/10.1145/3528223.3530071

Xuelin Chen, Honghua Li, Chi-Wing Fu, Hao Zhang, Daniel Cohen-Or, and Baoquan Chen. 2018a. 3D fabrication with universal building blocks and pyramidal shells. *ACM Transactions on Graphics* 37, 6 (dec 2018), 1–15. https://doi.org/10.1145/3272127.3275033

Xuelin Chen, Hao Zhang, Jinjie Lin, Ruizhen Hu, Lin Lu, Qixing Huang, Bedrich Benes, Daniel Cohen-Or, and Baoquan Chen. 2015. Dapper: decompose-and-pack for 3D printing. *ACM Transactions on Graphics* 34, 6 (nov 2015), 1–12. https://doi.org/10.1145/2816795.2818087

Chengkai Dai, Charlie C. L. Wang, Chenming Wu, Sylvain Lefebvre, Guoxin Fang, and Yong-Jin Liu. 2018. Support-free volume printing by multi-axis motion. *ACM Transactions on Graphics* 37, 4 (jul 2018), 1–14. https://doi.org/10.1145/3197517.3201342

Mohammadreza Lalegani Dezaki, Ahmad Serjouei, Ali Zolfagharian, Mohammad Fotouhi, Mahmoud Moradi, M.K.A. Ariffin, and Mahdi Bodaghi. 2022. A review on additive/subtractive hybrid manufacturing of directed energy deposition (DED) process. *Advanced Powder Materials* 1, 4 (oct 2022), 100054. https://doi.org/10.1016/j.apmate.2022.100054

Ugur M. Dilberoglu, Bahar Gharehpapagh, Ulas Yaman, and Melik Dolen. 2021. Current trends and research opportunities in hybrid additive manufacturing. *The International Journal of Advanced Manufacturing Technology* 113, 3-4 (jan 2021), 623–648. https://doi.org/10.1007/s00170-021-06688-1

Simon Duenser, Roi Poranne, Bernhard Thomaszewski, and Stelian Coros. 2020. Robocut: Hot-wire cutting with robot-controlled flexible rods. *ACM Transactions on Graphics (TOG)* 39, 4 (2020), 98–1.

Jimmy Etienne, Nicolas Ray, Daniele Panozzo, Samuel Hornus, Charlie C. L. Wang, Jonàs Martínez, Sara McMains, Marc Alexa, Brian Wyvill, and Sylvain Lefebvre. 2019. CurviSlicer: Slightly curved slicing for 3-axis printers. *ACM Transactions on Graphics* 38, 4 (jul 2019), 1–11. https://doi.org/10.1145/3306346.3323022

Guoxin Fang, Tianyu Zhang, Sikai Zhong, Xiangjia Chen, Zichun Zhong, and Charlie C. L. Wang. 2020. Reinforced FDM: multi-axis filament alignment with controlled anisotropic strength. *ACM Transactions on Graphics* 39, 6 (nov 2020), 1–15. https://doi.org/10.1145/3414685.3417834

SÁNDOR P. FEKETE and JOSEPH S. B. MITCHELL. 2001. Terrain Decomposition and Layered Manufacturing. *International Journal of Computational Geometry & Applications* 11, 06 (dec 2001), 647–668. https://doi.org/10.1142/s0218195901000687

Thomas Feldhausen, Lauren Heinrich, Kyle Saleeby, Alan Burl, Brian Post, Eric MacDonald, Chris Saldana, and Lonnie Love. 2022. Review of Computer-Aided Manufacturing (CAM) strategies for hybrid directed energy deposition. *Additive Manufacturing* 56 (aug 2022), 102900. https://doi.org/10.1016/j.addma.2022.102900

I. Filoscia, T. Alderighi, D. Giorgi, L. Malomo, M. Callieri, and P. Cignoni. 2020. Optimizing Object Decomposition to Reduce Visual Artifacts in 3D Printing. *Computer Graphics Forum* 39, 2 (may 2020), 423–434. https://doi.org/10.1111/cgf.13941

Joseph M. Flynn, Alborz Shokrani, Stephen T. Newman, and Vimal Dhokia. 2016. Hybrid additive and subtractive machine tools – Research and industrial developments. *International Journal of Machine Tools and Manufacture* 101 (feb 2016), 79–101. https://doi.org/10.1016/j.ijmachtools.2015.11.007

Qingzhe Gao, Bin Wang, Libin Liu, and Baoquan Chen. 2021. Unsupervised co-part segmentation through assembly. In *International Conference on Machine Learning*. PMLR, 3576–3586.

Yong Sheng Han, Bin Xu, Lei Zhao, and Yi Min Xie. 2019. Topology optimization of continuum structures under hybrid additive-subtractive manufacturing constraints. *Structural and Multidisciplinary Optimization* 60 (2019), 2571–2595.

George P. Harabin and Morad Behandish. 2022. Hybrid Manufacturing Process Planning for Arbitrary Part and Tool Shapes. *Computer-Aided Design* 151 (oct 2022), 103299. https://doi.org/10.1016/j.cad.2022.103299

Philipp Herholz, Wojciech Matusik, and Marc Alexa. 2015. Approximating Free-form Geometry with Height Fields for Manufacturing. *Computer Graphics Forum* 34, 2 (may 2015), 239–251. https://doi.org/10.1111/cgf.12556

Ruizhen Hu, Honghua Li, Hao Zhang, and Daniel Cohen-Or. 2014. Approximate pyramidal shape decomposition. *ACM Transactions on Graphics* 33, 6 (nov 2014), 1–12. https://doi.org/10.1145/2661229.2661244

Daphna Kaplan, Shir Rorberg, Mirela Ben Chen, and Yoav Sterman. 2022. NozMod: Nozzle Modification for Efficient FDM 3D Printing. In *Proceedings of the 7th Annual ACM Symposium on Computational Fabrication*. 1–9.

E. Karasik, R. Fattal, and M. Werman. 2019. Object Partitioning for Support-Free 3D-Printing. *Computer Graphics Forum* 38, 2 (may 2019), 305–316. https://doi.org/10.1111/cgf.13639

Alan C. Lin and Nguyen Huu Quang. 2014. Automatic generation of mold-piece regions and parting curves for complex CAD models in multi-piece mold design. *Computer-Aided Design* 57 (dec 2014), 15–28. https://doi.org/10.1016/j.cad.2014.06.014

Changqing Liu, Yingguang Li, Sen Jiang, Zhongyu Li, and Ke Xu. 2019a. A sequence planning method for five-axis hybrid manufacturing of complex structural parts. *Proceedings of the Institution of Mechanical Engineers, Part B: Journal of Engineering Manufacture* 234, 3 (nov 2019), 421–430. https://doi.org/10.1177/0954405419883052

Jikai Liu and Albert C. To. 2016. Topology optimization for hybrid additive-subtractive manufacturing. *Structural and Multidisciplinary Optimization* 55, 4 (aug 2016), 1281–1299. https://doi.org/10.1007/s00158-016-1565-4

Jikai Liu, Yufan Zheng, Yongsheng Ma, Ahmed Qureshi, and Rafiq Ahmad. 2019b. A Topology Optimization Method for Hybrid Subtractive–Additive Remanufacturing. *International Journal of Precision Engineering and Manufacturing-Green Technology* 7, 5 (mar 2019), 939–953. https://doi.org/10.1007/s40684-019-00075-8

Xin Liu, Chuhua Xian, Shuo Jin, and Guiqing Li. 2021. Surface attributes driven volume segmentation for 3D-printing. *Computers & Graphics* 100 (nov 2021), 43–53. https://doi.org/10.1016/j.cag.2021.07.020

Linjie Luo, Ilya Baran, Szymon Rusinkiewicz, and Wojciech Matusik. 2012. Chopper: partitioning models into 3D-printable parts. *ACM Transactions on Graphics* 31, 6 (nov 2012), 1–9. https://doi.org/10.1145/2366145.2366148

Ali Mahdavi-Amiri, Fenggen Yu, Haisen Zhao, Adriana Schulz, and Hao Zhang. 2020. VDAC: volume decompose-and-carve for subtractive manufacturing. *ACM Transactions on Graphics* 39, 6 (dec 2020), 1–15. https://doi.org/10.1145/3414685.3417772

Luigi Malomo, Nico Pietroni, Bernd Bickel, and Paolo Cignoni. 2016. FlexMolds: automatic design of flexible shells for molding. *ACM Transactions on Graphics* 35, 6 (nov 2016), 1–12. https://doi.org/10.1145/2980179.2982397

Jonàs Martínez, Haichuan Song, Jérémie Dumas, and Sylvain Lefebvre. 2017. Orthotropic k-nearest foams for additive manufacturing. *ACM Transactions on Graphics (TOG)* 36, 4 (2017), 1–12.

Alessandro Muntoni, Marco Livesu, Riccardo Scateni, Alla Sheffer, and Daniele Panozzo. 2018. Axis-Aligned Height-Field Block Decomposition of 3D Shapes. *ACM Transactions on Graphics* 37, 5 (oct 2018), 1–15. https://doi.org/10.1145/3204458

Kazutaka Nakashima, Thomas Auzinger, Emmanuel Iarussi, Ran Zhang, Takeo Igarashi, and Bernd Bickel. 2018. CoreCavity: interactive shell decomposition for fabrication with two-piece rigid molds. *ACM Transactions on Graphics* 37, 4 (jul 2018), 1–13. https://doi.org/10.1145/3197517.3201341

Sriram Pemmaraju and Steven Skiena. 2003. *Computational Discrete Mathematics: Combinatorics and Graph Theory with Mathematica*. Cambridge University Press. https://doi.org/10.1017/CBO9781139164849

SIEMENS. [n. d.]. SIEMENS NX 2206. https://www.plm.automation.siemens.com/. (Jan. [n. d.]).

Peng Song, Bailin Deng, Ziqi Wang, Zhichao Dong, Wei Li, Chi-Wing Fu, and Ligang Liu. 2016. CofiFab: coarse-to-fine fabrication of large 3D objects. *ACM Transactions on Graphics* 35, 4 (jul 2016), 1–11. https://doi.org/10.1145/2897824.2925876

Weiming Wang, Dirk Munro, Charlie CL Wang, Fred van Keulen, and Jun Wu. 2020. Space-time topology optimization for additive manufacturing: Concurrent optimization of structural layout and fabrication sequence. *Structural and Multidisciplinary Optimization* 61 (2020), 1–18.

Weiming M Wang, Cédric Zanni, and Leif Kobbelt. 2016. Improved surface quality in 3D printing by optimizing the printing direction. In *Computer graphics forum*, Vol. 35. Wiley Online Library, 59–70.

Ziqi Wang, Peng Song, and Mark Pauly. 2021. State of the Art on Computational Design of Assemblies with Rigid Parts. *Computer Graphics Forum* 40, 2 (may 2021), 633–657. https://doi.org/10.1111/cgf.142660

Chenming Wu, Chengkai Dai, Guoxin Fang, Yong-Jin Liu, and Charlie C. L. Wang. 2020a. General Support-Effective Decomposition for Multi-Directional 3-D Printing. *IEEE Transactions on Automation Science and Engineering* 17, 2 (apr 2020), 599–610. https://doi.org/10.1109/tase.2019.2938219

Chenming Wu, Yong-Jin Liu, and Charlie C. L. Wang. 2020b. Learning to Accelerate Decomposition for Multi-Directional 3D Printing. *IEEE Robotics and Automation Letters* 5, 4 (oct 2020), 5897–5904. https://doi.org/10.1109/lra.2020.3011369

Xinyi Xiao and Sanjay Joshi. 2020a. Decomposition and Sequencing for a 5-Axis Hybrid Manufacturing Process. In *International Manufacturing Science and Engineering Conference*, Vol. 84256. American Society of Mechanical Engineers, V001T01A049.

Xinyi Xiao and Sanjay Joshi. 2020b. Process planning for five-axis support free additive manufacturing. *Additive Manufacturing* 36 (dec 2020), 101569. https://doi.org/10.1016/j.addma.2020.101569

Ke Xu, Lufeng Chen, and Kai Tang. 2019. Support-Free Layered Process Planning Toward 3+2-Axis Additive Manufacturing. *IEEE Transactions on Automation Science and Engineering* 16, 2 (apr 2019), 838–850. https://doi.org/10.1109/tase.2018.2867230

Tianyu Zhang, Guoxin Fang, Yuming Huang, Neelotpal Dutta, Sylvain Lefebvre, Zekai Murat Kilic, and Charlie C. L. Wang. 2022. S^3-Slicer: A General Slicing Framework for Multi-Axis 3D Printing. *ACM Transactions on Graphics* 41, 6 (nov 2022), 1–15. https://doi.org/10.1145/3550454.3555516

Weijun Zhang, Masakazu Soshi, and Kazuo Yamazaki. 2020. Development of an additive and subtractive hybrid manufacturing process planning strategy of planar surface for productivity and geometric accuracy. *The International Journal of Advanced Manufacturing Technology* 109, 5-6 (jul 2020), 1479–1491. https://doi.org/10.1007/s00170-020-05733-9

Haisen Zhao, Hao Zhang, Shiqing Xin, Yuanmin Deng, Changhe Tu, Wenping Wang, Daniel Cohen-Or, and Baoquan Chen. 2018. DSCarver: decompose-and-spiral-carve for subtractive manufacturing. *ACM Transactions on Graphics* 37, 4 (aug 2018), 1–14. https://doi.org/10.1145/3197517.3201338

Fanchao Zhong, Yonglai Xu, Haisen Zhao, and Lin Lu. 2022. As-continuous-as-possible Extrusion-based Fabrication of Surface Models. *ACM Transactions on Graphics* (dec 2022). https://doi.org/10.1145/3575859